Smart Materials and Structures

PURPOSE-LED PUBLISHING™

PAPER • OPEN ACCESS

The effect of microstructural barriers on transient crack growth in shape memory alloys

To cite this article: Fatma Mutlu *et al* 2023 *Smart Mater. Struct.* **32** 095006

View the article online for updates and enhancements.

You may also like

- Subcritical fatigue in fuse networks
C. L. N. Oliveira, A. P. Vieira, H. J. Herrmann et al.
- Study of fractography of ferritic ductile iron at different temperatures and loading conditions
Wenjie Wang, Zekun Wang, Zhiren Sun et al.
- Fracture behavior of polyvinyl alcohol fiber reinforced concrete: an experimental and numerical study based on DIC
Wanming Yang, Xiaolin Yang, Lin He et al.

This content was downloaded from IP address 193.140.199.113 on 19/03/2026 at 07:13

OPEN ACCESS
IOP Publishing
Smart Materials and Structures
Smart Mater. Struct. **32** (2023) 095006 (18pp)
https://doi.org/10.1088/1361-665X/ace74d

The effect of microstructural barriers on transient crack growth in shape memory alloys

Fatma Mutlu[1,*], **Günay Anlaş**[1] and **Hüseyin Şehitoğlu**[2]

[1] Department of Mechanical Engineering, Boğaziçi University, South Campus, Bebek, Beşiktaş, İstanbul 34342, Turkey
[2] Department of Mechanical Science and Engineering, University of Illinois at Urbana-Champaign, 1206 W. Green St., Urbana 61801, IL, United States of America

E-mail: fatma.mutlu@boun.edu.tr

Received 9 March 2023, revised 4 July 2023
Accepted for publication 13 July 2023
Published 24 July 2023

Abstract

There are several issues to be solved in the fracture mechanics of shape memory alloys, one of them being the resistance to crack growth and therefore to fracture. This paper discusses the crack growth in a single crystal CoNiAl shape memory alloy under cyclic loading and the effect of micro-structural barriers. To observe the crack growth in detail, tests are conducted on edge-notched specimens. The displacement field is obtained using digital image correlation (DIC), and the fracture parameters are calculated by fitting anisotropic crack tip displacement equations to DIC data. Similar crack growth behaviors are observed in both superelastic and shape memory specimens, with a comparatively higher crack growth rate in the superelastic case: first a crack initiates at the notch and grows, then new cracks are observed to form near the tip of the main crack, or on the notch when the growth slows down. Then, further cyclic loading leads to the growth of the main crack and the new crack simultaneously with the two cracks merging at the end. Test specimens are examined post-failure with optical microscopy to better understand this complicated behavior. Results showed the presence of a non-transforming secondary (γ) phase around the regions where the propagating cracks slowed down, deviated, and/or stopped, improving the resistance of the shape memory alloy specimen to fracture.

Keywords: shape memory alloys, superelasticity—shape memory effect, single crystal CoNiAl, fatigue crack growth, microstructural barriers, digital image correlation

(Some figures may appear in colour only in the online journal)

1. Introduction

This paper aims to study the fatigue crack growth in anisotropic shape memory alloys with an emphasis on the behavior in the presence of a secondary phase. In the literature, there are a few studies on propagating crack-γ phase interaction in shape memory alloys [1–3]: Ma *et al* [1] and Wu *et al* [2] report an increase in fracture toughness of NiMnCoGa, NiMnSnFe, but do not calculate any corresponding fracture parameters. Euh *et al* [3] work on NiMnGaFe and calculate the stress intensity factors but only when the crack tip is located inside the γ-phase and under quasi-static loading; they do not evaluate the crack growth under cyclic loading. In this work, the effect of a secondary phase that acts as a microstructural barrier in a single crystal shape memory alloy is investigated for the first time by studying in detail the crack growth under cyclic loading in a single crystal shape memory alloy, CoNiAl,

* Author to whom any correspondence should be addressed.

Original Content from this work may be used under the terms of the Creative Commons Attribution 4.0 licence. Any further distribution of this work must maintain attribution to the author(s) and the title of the work, journal citation and DOI.

 © 2023 The Author(s). Published by IOP Publishing Ltd

which is brittle in nature and is prone to brittle cracking. In the literature, although there is a number of works on functional fatigue [4–7], studies on fracture mechanics of CoNiAl lack.

The sample material CoNiAl is subjected to heat treatment which resulted in a secondary phase (γ-phase) with the volume fraction depending on the annealing temperature, its duration, and the rate of cooling. The heat treatment modified the transformation temperatures A_s, M_s, A_f, and M_f and the shape memory and superelastic behavior [8–12] (a shape-memory behavior at room temperature, and a superelastic behavior at 50 °C under tensile loading). The presence of the γ-phase also increases the transformation strains [4, 8–11, 13–15] and affects the tensile strength, ductility, superelastic properties and shape memory strain recovery capabilities of the alloy [10, 16–18]. The secondary phase does not undergo forward martensitic transformation or re-orientation [19].

The mechanical behavior of single crystal CoNiAl SMAs depends on the crystallographic orientation; the transformation stresses, transformation temperatures, and cyclic stability under tension and compression loads are all crystallographic orientation dependent [20, 21].This study focuses on the [100] orientation, which has fewer available slip systems than the other orientations, resulting in a harder slip activation. It has been reported that the insufficiency of dislocations due to harder activation of slip systems might delay phase transformation but provide almost perfect superelasticity, with lower residual strains than any other orientation [11, 21].

To study the crack growth in detail, crack growth tests are performed on edge-notched CoNiAl specimens. Cyclic loading tests are conducted in superelastic and shape memory regimes to determine the fatigue crack growth in specimens with two distinct crystalline phases: the austenitic phase that transforms to martensitic phase and the martensitic phase that undergoes re-orientation. The details of the experiments are given in section 2. Full-field displacement data obtained with DIC are fitted to the equations for the anisotropic displacement field around the crack tip, and the fracture parameters are calculated at each step of the growing crack. Specimens that are subjected to cyclic loading are examined post-failure with optical microscopy to determine the transient crack growth behavior.

2. Experiments

CoNiAl samples that are cut using electric discharge machining (EDM) from single crystal $Co_{36}Ni_{35}Al_{29}(at.\%)$ bulk material (grown using the Bridgman technique in an inert environment) are used. The [100] crystallographic orientation is chosen for the experiments.

The test specimens are homogenized at 1275 °C for 24 h in a vacuum furnace, and left to cool in air. After the heat treatment, the material exhibits shape memory behavior at room temperature ($T = 20$ to 25 °C), and superelastic behavior at T = 50 °C in tension. The microstructure consists of a cobalt-rich secondary (γ) phase, and a matrix which is austenitic crystal in the superelastic case, and martensitic upon transformation. The secondary phase does not undergo any phase transformation or re-orientation [19].

All specimens are polished to a mirror surface finish using SiC paper up to P4000 and 1 μm suspended alumina, and a fine speckle pattern is obtained by air blasting 1000 grit SiC powder on the polished surface for full-field displacement and strain measurements using DIC. The experiments are conducted using a servo-hydraulic load frame equipped with a digital controller, and a computer program is used to control the load frame and to synchronize the acquisition of the DIC images that are captured with a charge-coupled device (CCD) camera. The digital camera has a resolution of 1600 × 1200 pixels, with a maximum frame rate of 15 fps, and an adjustable lens with a 12X magnification range and a 2X adapter. For the image correlation and strain calculations, commercial software—Vic2d from Correlated Solutions, is used. Strains are monitored with DIC during the entire loading and unloading process.

To understand the mechanical behavior of the material, dog-bone specimens are used, specimens have a width = 2.93 mm, a thickness = 1.38 mm, and a gauge length = 8 mm. Displacement-controlled tension tests are conducted to observe the superelastic and shape memory behavior and the hysteresis. Strains are calculated from DIC images taken at 2 s intervals. The specimen used for the superelastic case is heated to 50 °C using heating tapes and loaded in tension under position control to 0.25 mm elongation; the second test is conducted at room temperature ($T = 20$ °C), and the specimen is loaded under position control to 0.2 mm elongation.

2.1. Crack growth measurements & DIC

For the crack growth experiments, five 8-mm long edge-notched dog-bone specimens with an edge notch cut at the mid-section are used, a sketch of which is shown in figure 1. The first superelastic (SE1) specimen has a gauge section width of 2.88 mm and a thickness of 1.32 mm; the second superelastic (SE2) specimen has a gauge section width of 2.93 mm, a thickness of 1.32 mm; the shape memory (SM) specimen has a width of 2.93 mm and a thickness of 1.35 mm. Each edge notch is 0.5 mm long and is cut using EDM with a 0.1778 mm diameter wire.

Stress-controlled experiments are conducted at 50 °C at 3 Hz frequency, under a constant stress amplitude of 80.75 MPa with an $R = 0.05$ for the two superelastic cases, and at room temperature (25 °C), under 57 MPa for the shape memory one. Crack initiation and subsequent growth are monitored during each cycle using a CCD camera focused on the area around the notch/crack tip. The displacement field that is extracted from the images is used to locate the sharp crack tip. After the initiation of a crack, the loading frequency is reduced to 0.2 Hz, images around the crack tip are taken with the same CCD camera, and DIC data are collected.

The stress intensity factors, ΔK_I and ΔK_{II}, are determined by fitting the displacement data obtained from DIC to the crack

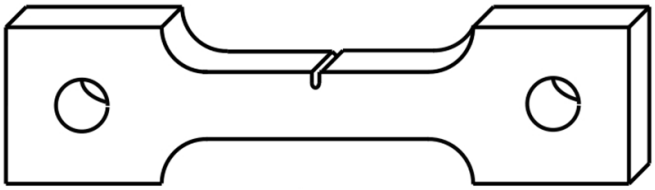


Figure 1. Edge-notched dog bone specimen. A 0.5 mm notch is cut at the midsection.

tip displacement equations proposed by Sih *et al* [22] for linear elastic anisotropic bodies, following a similar procedure to [23, 24]:

$$\begin{aligned}\Delta u =& \Delta K_I\sqrt{\frac{2r}{\pi}}Re\left[\frac{1}{\mu_1-\mu_2}\left(\mu_1 p_2\sqrt{\cos\theta+\mu_2\sin\theta}\right.\right.\\&\left.\left.-\mu_2 p_1\sqrt{\cos\theta+\mu_2\sin\theta}\right)\right]\\&+\Delta K_{II}\sqrt{\frac{2r}{\pi}}Re\left[\frac{1}{\mu_1-\mu_2}\left(p_2\sqrt{\cos\theta+\mu_2\sin\theta}\right.\right.\\&\left.\left.-p_1\sqrt{\cos\theta+\mu_2\sin\theta}\right)\right]\\&+a_{11}Tr\cos\theta-Ar\sin\theta+B_u,\end{aligned}\tag{1}$$

$$\begin{aligned}\Delta v =& \Delta K_I\sqrt{\frac{2r}{\pi}}Re\left[\frac{1}{\mu_1-\mu_2}\left(\mu_1 q_2\sqrt{\cos\theta+\mu_2\sin\theta}\right.\right.\\&\left.\left.-\mu_2 q_1\sqrt{\cos\theta+\mu_2\sin\theta}\right)\right]\\&+\Delta K_{II}\sqrt{\frac{2r}{\pi}}Re\left[\frac{1}{\mu_1-\mu_2}\left(q_2\sqrt{\cos\theta+\mu_2\sin\theta}\right.\right.\\&\left.\left.-q_1\sqrt{\cos\theta+\mu_2\sin\theta}\right)\right]\\&+a_{12}Tr\sin\theta+Ar\cos\theta+B_v,\end{aligned}\tag{2}$$

where

$$p_i = a_{11}\mu_i^2 + a_{12} - a_{16}\mu_i,\tag{3}$$

$$q_j = a_{12}\mu_j + \frac{a_{22}}{\mu_j} - a_{26},\tag{4}$$

and

$$a_{11}\mu^4 - 2a_{16}\mu^3 + (2a_{12}+a_{66})\mu^2 - 2a_{26}\mu + a_{22} = 0.\tag{5}$$

In the equations above Re represents the real part of a complex number, A is the rigid body rotation, B_u and B_v are the rigid body translations in u and v directions, respectively. T is the T-stress [25]. The inclusion of the T-stress is needed for better accuracy in the calculation of fracture parameters [26]. $a_{11}, a_{12}, a_{16}, a_{22}, a_{26}$, and a_{66} are the reduced compliance components for plane stress problems, and μ_1 and μ_2 are the complex roots of equation (5). The coordinate system used is shown in figure 2. The stress intensity factors, ΔK_I and ΔK_{II}, as well as the T-stress and rigid body motion terms are extracted from equations (1) and (2). The effective stress intensity factor ΔK_{eff} for mixed-mode is calculated as follows:

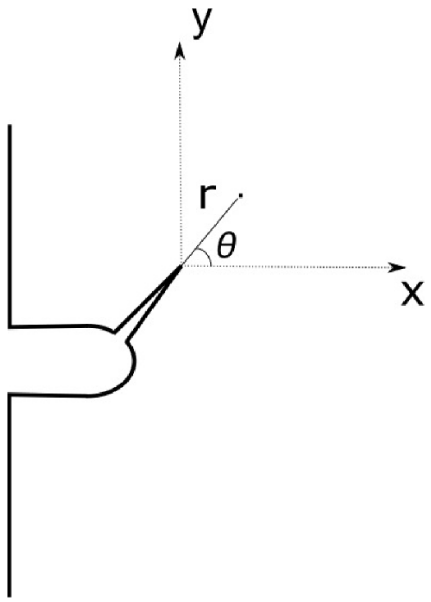


Figure 2. Crack tip configuration presented in polar coordinates.

$$\Delta K_{\text{eff}} = \sqrt{K_I^2 + \alpha K_{II}^2}\tag{6}$$

where

$$\alpha = \frac{\Delta J_2}{\Delta J_1}, \quad \text{and}\tag{7}$$

$$\Delta J_1 = -\frac{\pi\Delta K_I}{2}a_{22}Im\left[\frac{\Delta K_I(\mu_1+\mu_2)+\Delta K_{II}}{\mu_1\mu_2}\right]\tag{8}$$

$$\Delta J_2 = \frac{\pi\Delta K_{II}}{2}a_{11}Im\left[\Delta K_{II}(\mu_1+\mu_2)+\Delta K_I\mu_1\mu_2\right]\tag{9}$$

and μ_k are the roots of the characteristic equation (5). ΔJ_i in equations (8) and (9) are the energy release rates that are used to calculate the effective stress intensity factor, ΔK_{eff}, for mixed-mode [22].

In the calculations the compliance matrix components, $a_{11}, a_{16}, a_{12}, a_{66}, a_{26}$ and a_{22} that are not known are determined together with the fracture parameters using the least squares curve fitting of the DIC data to equations (1) and (2). Equations (3)–(5) are used as constraints.

3. Results and discussion

3.1. Stress–strain behavior

In figure 3 the superelastic stress & strain curve is plotted. The strains are extracted from a region where they are maximum,

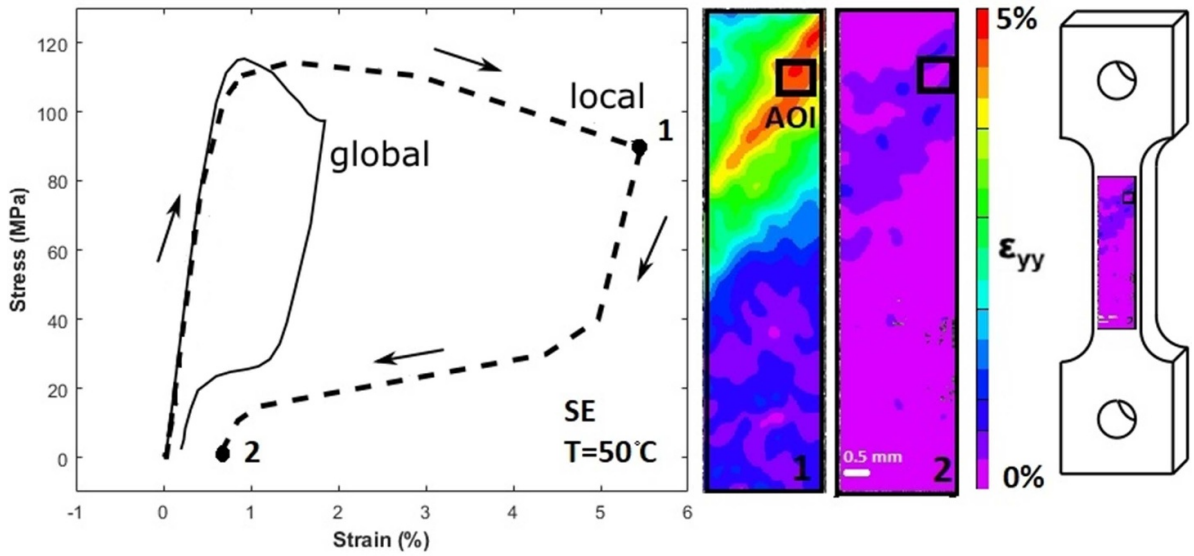


Figure 3. Stress–local strain behavior of the superelastic specimen (SE), $T = 50\,^{\circ}$C in tension. The strain is calculated from the mean of ϵ_{yy} extracted from the black framed region (AOI).

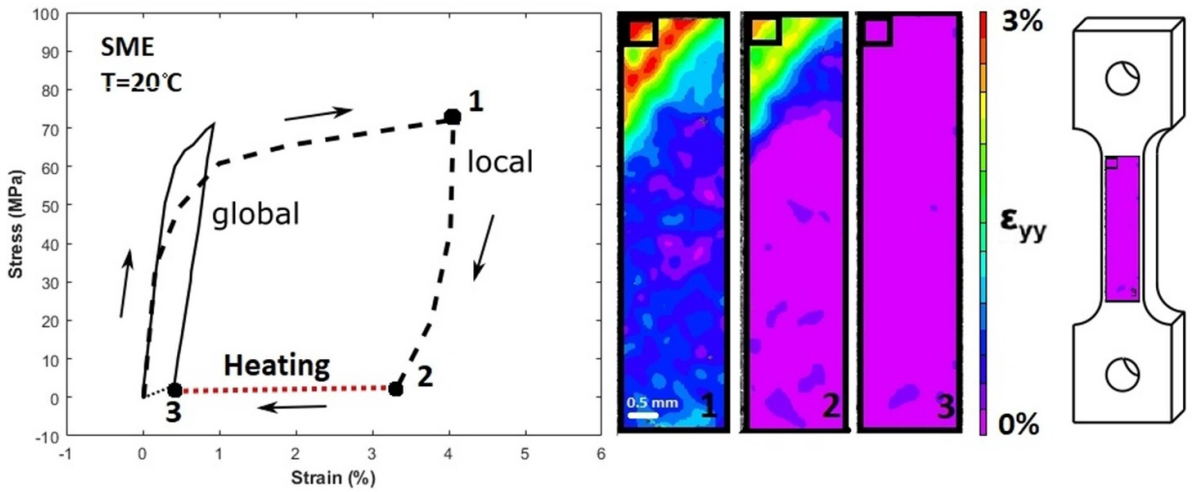


Figure 4. Stress–local strain behavior of the shape memory specimen (SM), $T = 20\,^{\circ}$C. The strain is calculated from the mean of the strains, ϵ_{yy}, extracted from the black-framed region.

namely the area of interest (AOI), shown with the black rectangle. A strain recovery of more than 90% proves a superelastic behavior; the material was in the austenitic phase at the beginning of the experiment and underwent a martensitic transformation with the forward transformation that started around 115 MPa.

The stress–strain curve of the shape memory case is plotted in figure 4. The local strains belong to the region shown with the black frame, where a strain localization occurs. The material is in the martensitic phase and undergoes re-orientation with loading as a result of the shape memory behavior. The martensitic re-orientation starts around a stress of 60 MPa. When the load is removed, the strain recovery is lower than 25% of the maximum strain ($1 \rightarrow 2$), which is then reduced to almost zero with heating to $100\,^{\circ}$C ($2 \rightarrow 3$).

3.2. Crack growth results

For the crack growth experiments, five edge-notched dog-bone specimens with edge-notches cut at the mid-sections are used. Three superelastic and two shape memory cyclic loading tests are conducted, and similar cracking behaviors are observed in superelastic and shape-memory regimes with the only differences being on gamma phase locations. As a result, two different test results of superelastic specimens, and one test

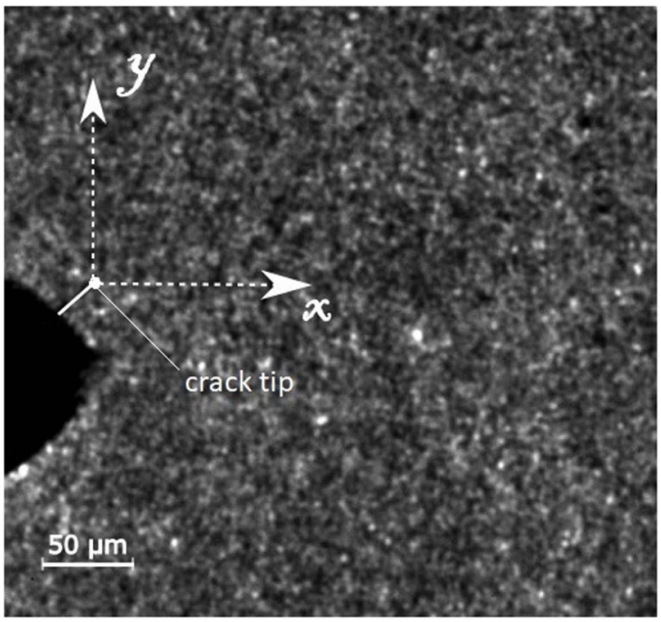


Figure 5. Crack initiation in the first superelastic specimen (SE1): Crack length = 0.027 mm, $\Delta K_{\text{eff}} = 6.10\,\text{MPa}\sqrt{\text{m}}$.

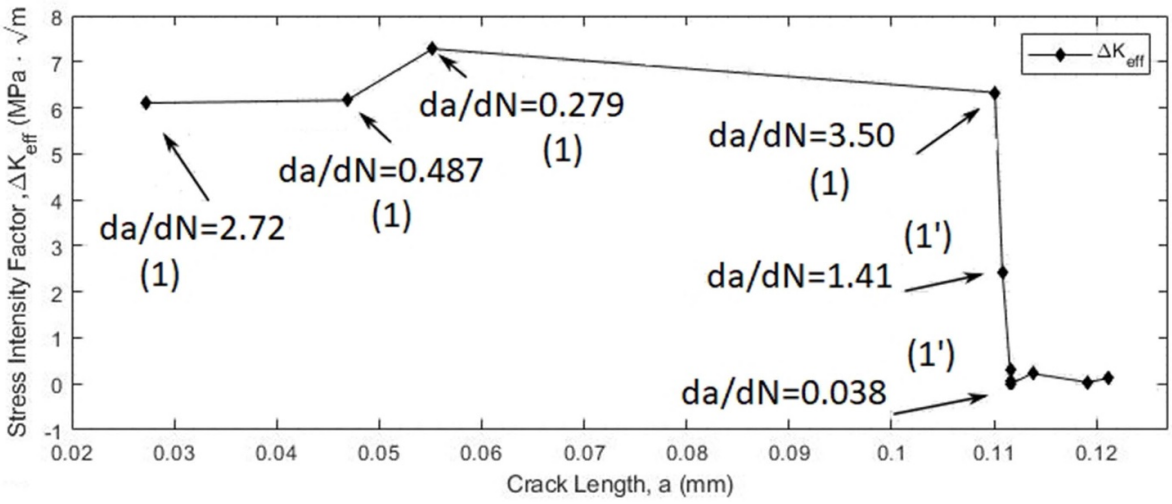


Figure 6. Effective stress intensity factor vs. crack length after crack initiation (SE1). Corresponding crack growth rates (da/dN) are given in 10^{-8} m cycle^{-1}. Numbers in parentheses correspond to the effective crack in the crack growth sequence in figure 7.

result of shape memory specimen are reported in the present work.

3.3. Superelastic case 1

In the first superelastic specimen, the crack initiated at the notch making an angle of $\approx 43°$ with the x-coordinate as shown in figure 5 after around 18 000 loading cycles. The effective stress intensity factor at crack initiation is calculated to be 6.1 MPa $\sqrt{\text{m}}$ for a crack length of 0.027 mm.

After initiation, the crack grows in the '1' direction with increasing stress intensity factor (see figure 6). During propagation, the crack growth rate drops to 0.487×10^{-8} m cycle^{-1} then to 0.279×10^{-8} m cycle^{-1}, which occurs upon hitting a small $\gamma-$phase region. The propagation slows down, the crack passes through the $\gamma-$phase region without kinking (figures 7 and 8). Then, when a crack length of 0.11 mm is reached, a sharp drop in the stress intensity factor is found, and the main crack is observed to kink from direction '1' to '1′′' as shown in figures 7 and 8. Then, the crack advanced slowly to '1′′′' with decreasing da/dN and comparatively lower stress intensity factors (figure 6).

In figures 8(a)–(c), the snapshots from the DIC camera show the growth of the crack. The first image in figure 8(a), is taken when the crack is 0.1479 mm long. Subsequent images are taken with intervals of 1000 cycles. When studied with figure 6, it is observed that when the crack changes direction (figure 8(a), '1' to '1′'), the stress intensity factor decreases. Later the crack continues to grow parallel to the initial crack following direction '1′′' with an increasing stress intensity

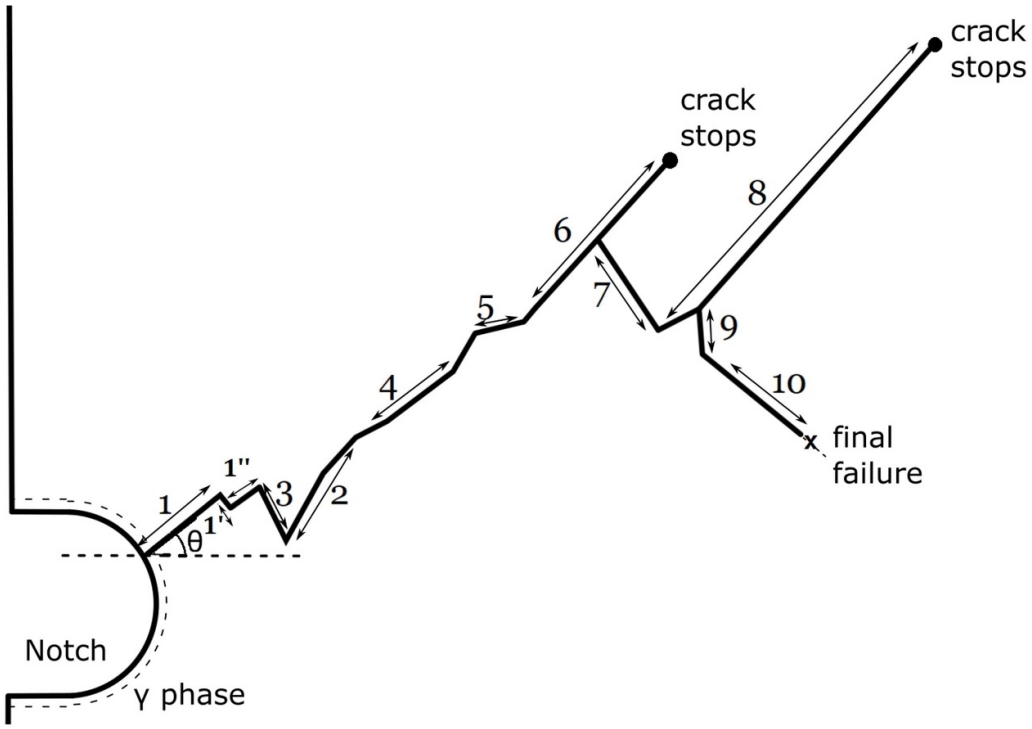


Figure 7. Sketch of crack growth path from the notch (SE1). Numbers indicate sequences of crack growth. The γ-phase region around the notch is shown by the dashed line. The specimen fails at ≈36 000 cycles.

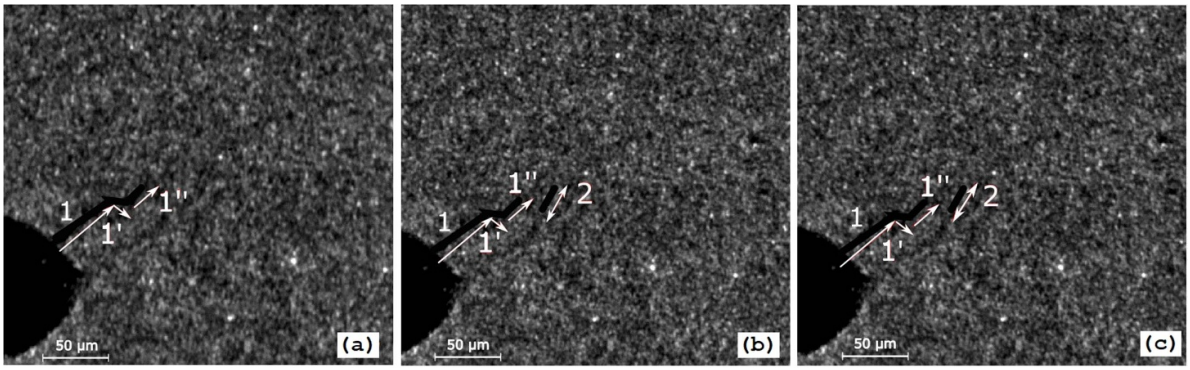


Figure 8. Crack initiation and following advancement in the first superelastic specimen (SE1). (a) DIC image showing kinking in the crack growth direction (‘1’ → ‘1′’ → ‘1′′’). (b) New crack forms (‘2’). (c)‘1′′’ and ‘2’ advance.

factor (figure 9). The first datum point in figure 9 corresponds to the last one in figure 6.

Stress intensity factor for figure 8(a) is calculated as 17.4 MPa$\sqrt{\text{m}}$, after which the main crack length (‘1’, ‘1′’ and ‘1′′’ in figure 8(b)) increases to 0.1502 mm, but the effective stress intensity factor decreases. As shown in figure 8(b), a new crack (‘2’) is observed to form, which explains the decrease in the stress intensity factor of the main crack (shown with ‘1′′’ in figure 9). During this period (‘1′′’ to ‘3’), the main crack continues growing. Still, the crack growth rate (da/dN) decreases, which is a result of the simultaneous growth of the two cracks: The new crack ‘2’ and the main crack from ‘1′′’. In figure 8(c), the newly formed crack ‘2’ slightly increases in size, extending from both ends: Upwards direction and downwards to the main crack ‘1′′’. Eventually, it merges with the main crack at the ‘3’ region as shown in figure 7. The stress intensity factor calculated for this case, where cracks ‘1′′’ and ‘2’ both continue growing independently, is calculated to be 1.5 MPa$\sqrt{\text{m}}$, and the main crack length increases to 0.1519 mm (figure 9).

For further analysis of this complicated and interesting crack behavior, the DIC paint on the surface of the specimen is cleaned and the specimen is examined under optical microscope after failure. Figure 10 shows the optical image of the ruptured specimen. It is observed that the stress intensity factor starts to decrease when the crack tip (‘1’) hits the boundary of the γ-phase. The initial crack is shown with an arrow numbered ‘1’ in figure 8 which kinks and continues

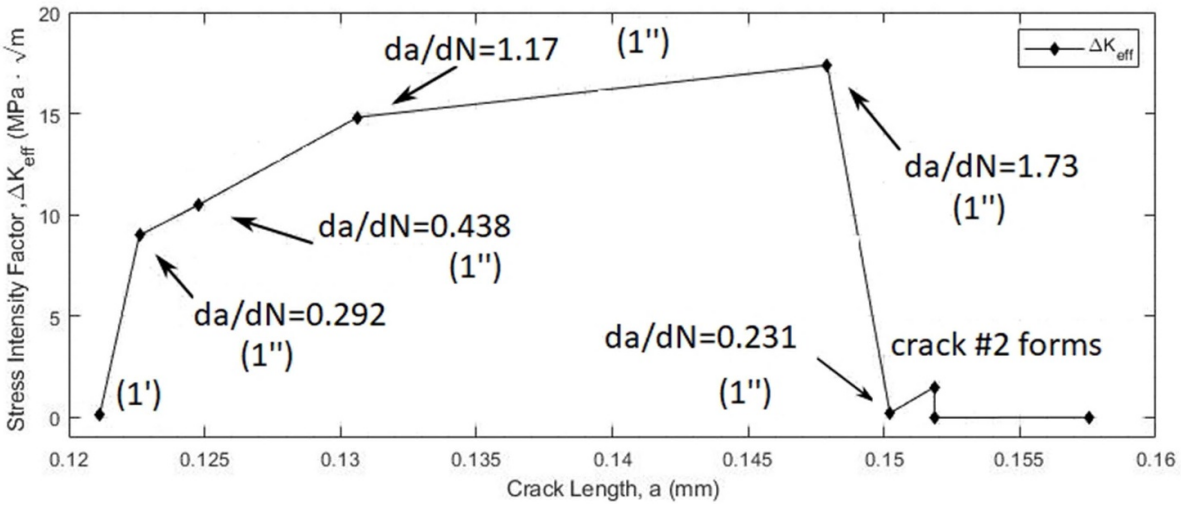


Figure 9. Effective stress intensity factor vs. crack length (SE1). Corresponding crack growth rates (da/dN) are given in 10^{-8} m cycle^{-1}. Numbers in parentheses correspond to the effective crack in the crack growth sequence in figure 7.

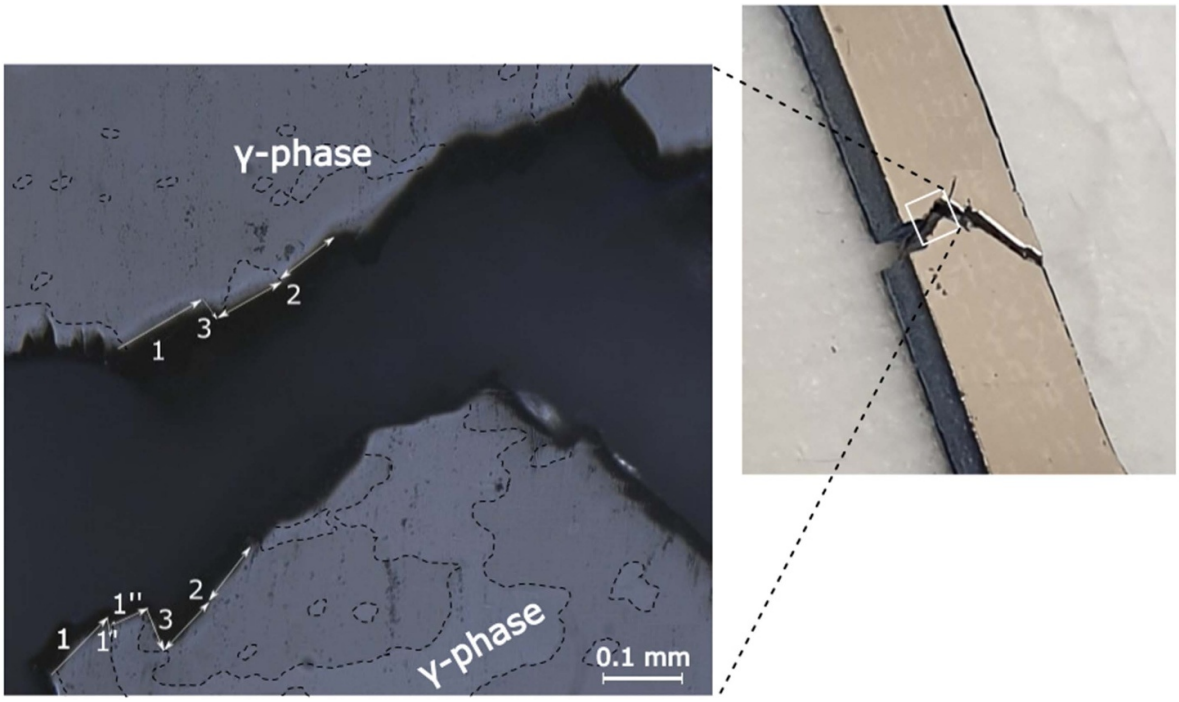


Figure 10. Optical microscopy image of the specimen SE1 taken after failure showing the cracks '1$^{''}$' and '2' merging at '3'. γ-phase borders are shown with black dashed lines. Inset shows the ruptured specimen and the area to which the microscopic image corresponds.

to grow parallel to the γ-phase boundary ('1$^{'}$'). Following another kink, it advances into the γ-phase and becomes '1$^{''}$'. From '1$^{'}$' to '1$^{''}$' the stress intensity factor increases as shown in figure 9. The arrow '2' in figure 10 corresponds to the new crack formation in figure 8(b). It first propagates upwards, then starts growing backwards towards the main crack ('1$^{''}$') after hitting the γ-phase region as shown in figure 10. Following further loading, the main crack '1$^{''}$' and the new crack '2' merge at '3' which happens to coincide with the boundary of the γ-phase. Effective stress intensity factors calculated during '1$^{''}$' to '3' are very low, which increase after merging.

In summary, what we see is, cracks stop, their directions deviate by the presence of γ-phase. In figure 11, two of the stopping cracks at the γ-phase boundaries can be seen. Initially the main crack advances through direction '6' which stops upon hitting the γ-phase boundary. It then continues to grow in direction '7'. '8' which also stops, later advances in direction '10'.

Additionally, microscopic inspections of the notch show that the notch edge itself is fully covered with the γ-phase that does not have an uniform thickness as shown in figure 12. The crack initiates inside the γ-phase (arrow 'i'), and only after

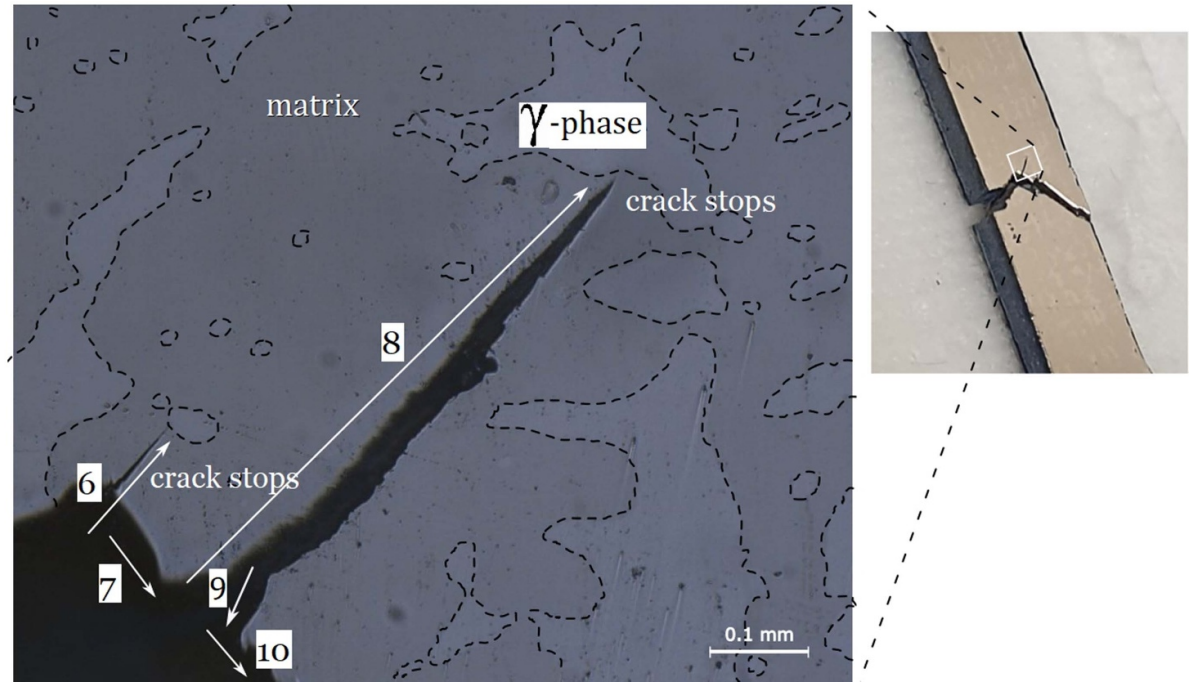


Figure 11. Cracks stop at γ-phase boundaries. Inset shows the ruptured specimen and the area to which the microscopic image corresponds (SE1). Numbers correspond to the effective crack in the crack growth sequence given in figure 7.

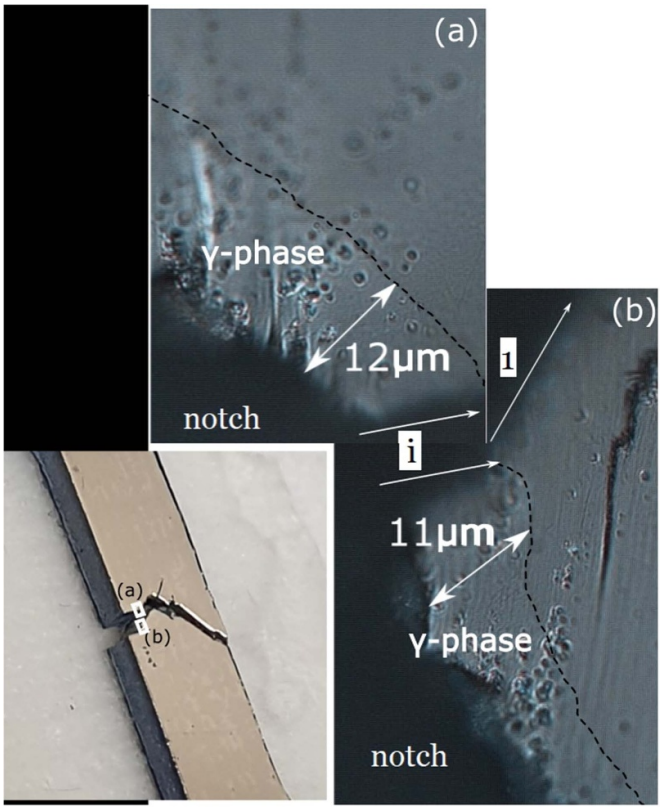


Figure 12. Microscopic images around the ruptured notch showing γ-phase (SE1). (a) the top with γ-phase thickness of $\approx 12\,\mu$m, (b) the bottom with $\approx 11\,\mu$m thickness.'i' indicates crack initiation inside γ-phase, and '1' corresponds to the first crack in figure 7.

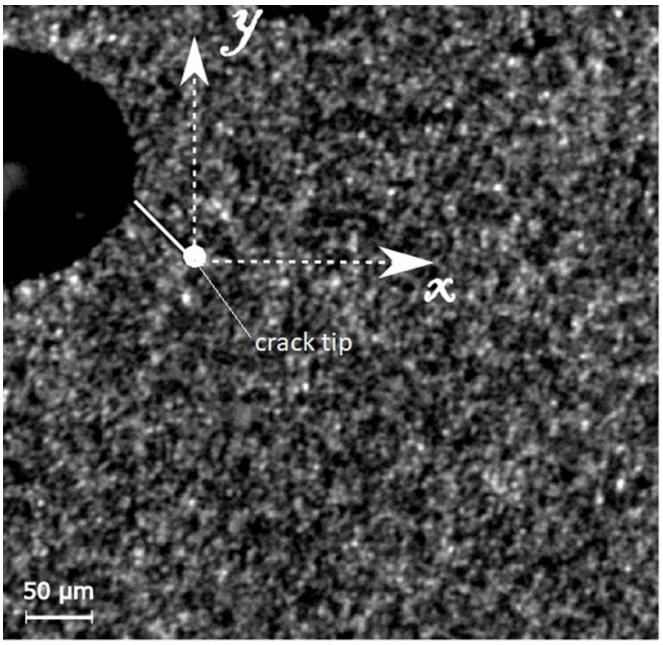


Figure 13. Crack initiation in the second superelastic specimen (SE2): Crack length = 0.0246 mm, $\Delta K_{\text{eff}} = 2.51\,\text{MPa}\sqrt{\text{m}}$.

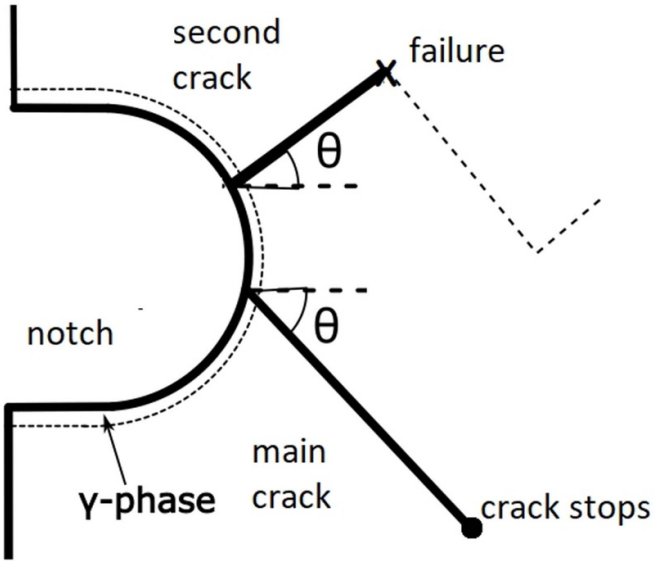


Figure 14. Sketch of the crack advancement (SE2): Cracks initiate and advance from the notch as shown. Dotted line around the notch shows the γ-phase region. The specimen fails from the 'second crack' when the crack length is 0.095 mm, and 1664 cycles after crack the initiation.

tearing through the γ-phase that it advances into the martensitic phase (arrow '1').

3.4. Superelastic case 2

A new experiment is conducted following similar conditions to the first one using the second superelastic specimen (SE2). This time the crack initiates at the notch at an angle of $\approx -42^\circ$ after 3000 cycles as shown in figure 13, keeping approximately the same magnitude of crack initiation angle seen in the first specimen (SE1). The effective stress intensity factor at crack initiation is calculated as $2.51\,\text{MPa}\sqrt{\text{m}}$ for a crack length of 0.0246 mm, significantly lower than the one calculated for the first specimen.

After initiation, the main crack is observed to advance faster than the growth observed in the first superelastic case until it stops at a length of 0.2012 mm after following a relatively straight path as presented with a sketch in figure 14.

Effective stress intensity factors increase to $10.8\,\text{MPa}\sqrt{\text{m}}$ during the advancement of the main crack. The effective stress intensity factors vs. crack length is plotted in figure 15.

When the DIC images are examined post failure, another crack is detected at the notch at $\approx 44^\circ$ angle (see the inset in figure 16) at the time when the main crack growth started to

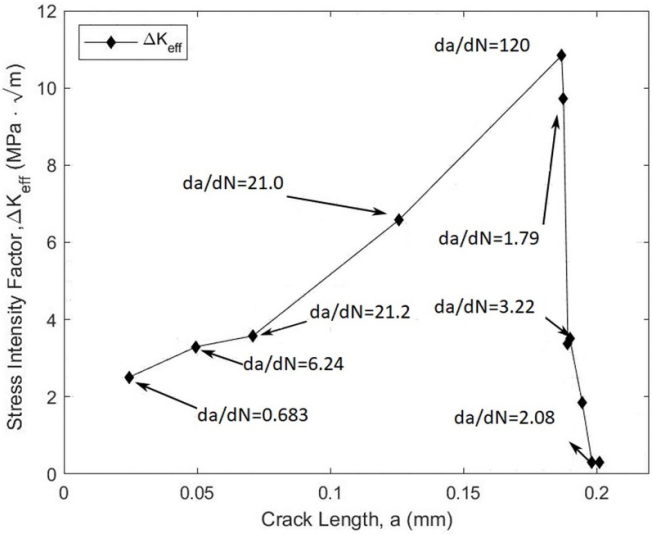


Figure 15. Effective stress intensity factor vs. crack length (SE2). Corresponding crack growth rates (da/dN) are given in 10^{-8} m cycle^{-1}. Results are for the main crack obtained from the area (AOI) that is shown in figure 16.

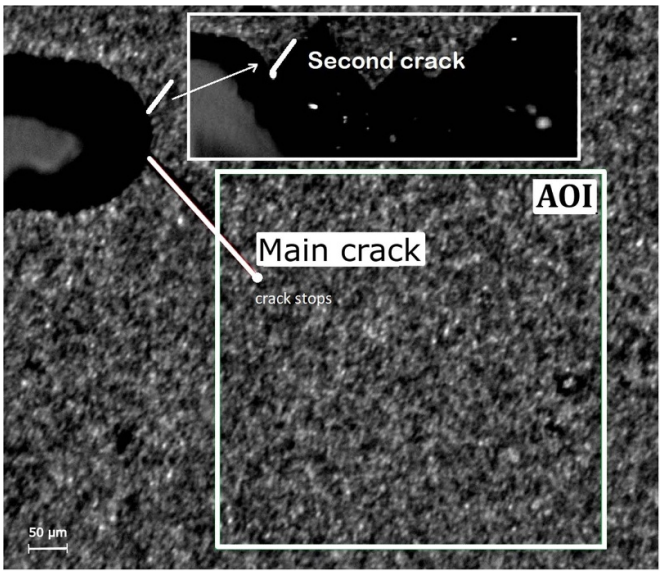


Figure 16. DIC image just before failure (SE2). Inset shows the DIC image of the second crack after failure.

slow down. This new crack grows faster than the main crack and the specimen finally fails from it, the advancement of this crack is sketched in figure 14 as 'second crack' together with the main crack. In figure 16, the main crack, the second crack, and the AOI, from which the data are collected during testing are shown. An image of the region after failure is added to show how the failure occurs from the second crack. The time increment between these images is 0.2 s.

To determine the effect of microstructural barrier on crack growth, the DIC paint is cleaned from the surface of the specimen, and the ruptured piece is examined under optical microscope. No γ-phase is observed around the crack tip as shown in figure 17 when the crack stops.

The formation of a new crack ('second crack') results in a decrease in the SIF calculated for the main crack, and the da/dN decreases from 120 to $1.79 \cdot 10^{-8}$ m cycle^{-1} (see figure 15). Later, the da/dN of the 'main crack' increases from 1.79 to $3.22 \cdot 10^{-8}$ m cycle^{-1}, which is found to be a result of a γ-phase encounter of the 'second crack' that stops momentarily. During this period, the 'main crack' continues to grow for 14.4 μm, then stops when the 'second crack' kinks and continues growing.

When the growth stops, the equivalent strain $\left(\epsilon_{eq} = \sqrt{\frac{2}{3}(\epsilon_{xx}^2 + \epsilon_{yy}^2 + 2\epsilon_{xy}^2)}\right)$ calculated from the DIC strain data is examined. Figure 18(a) shows that strains higher than 1% spread over a large area, indicating a martensitic transformation. After the crack stops, the region around the crack tip continues to transform. Figure 18(b) shows the equivalent strain contours after $\approx$ 300 loading cycles following the arrest of the crack and the area inside 1% strain contour is considerably larger than the one shown in figure 18(a).

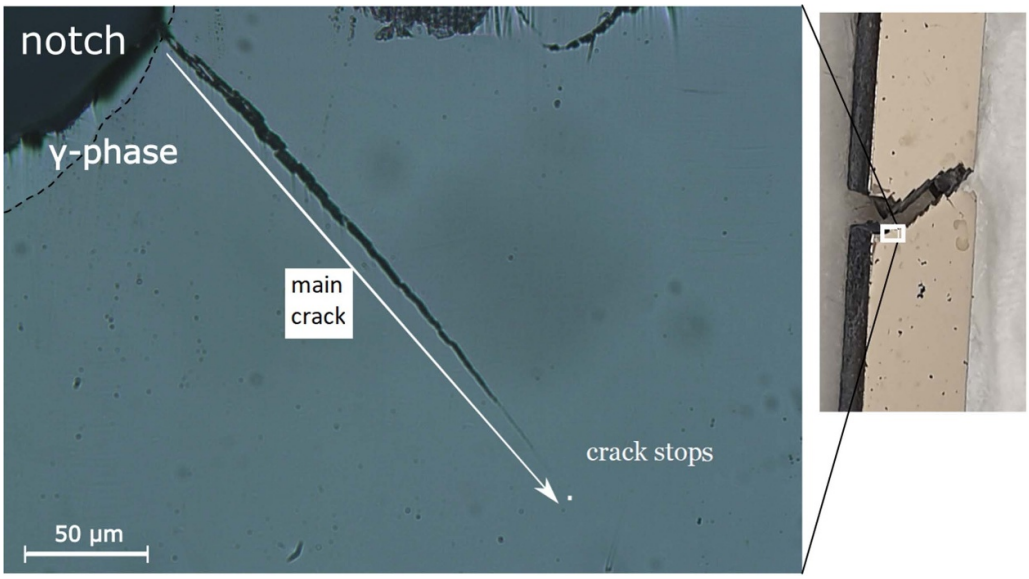


Figure 17. Optical microscopy of the main crack (SE2). γ-phase borders at the notch are shown with black dashed lines. Inset shows the ruptured specimen, and the area to which the microscopic image corresponds.

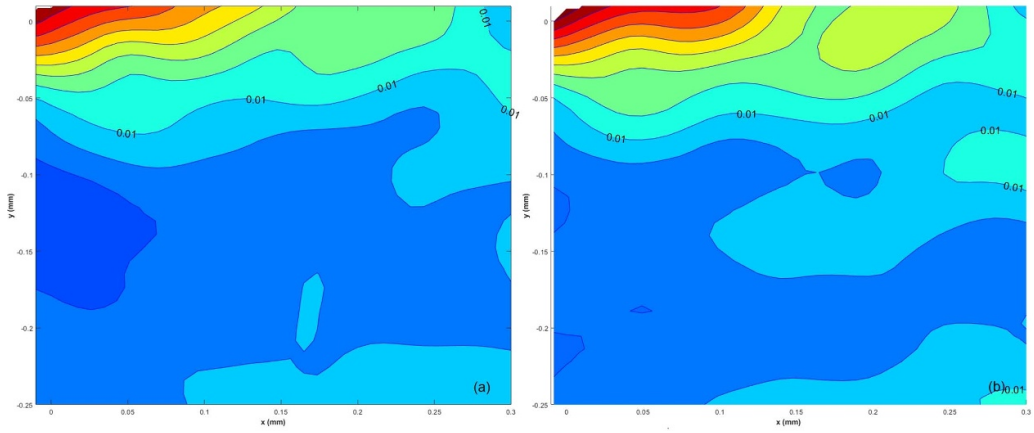


Figure 18. Equivalent strain (ϵ_{eq}) plots around the main crack tip after the crack stops (SE2). (a) Just after crack stops, (b) ≈300 cycles after crack stops. Results are obtained from the AOI in figure 16.

Next, the region around the notch is inspected in the ruptured specimen. In figure 19 the images from the optical microscope of the two cracks formed at the notch are presented (also see figure 14). The initiation point of the main crack at the notch is given in figure 19(b), and figure 19(a) shows the second crack. The size of the γ-phase in figure 19(a) is larger around the initiation point of the second crack than the one shown in figure 19(b). The DIC images show that the 'second crack' initiates first at the notch. But owing to the smaller area of γ-phase at the crack tip, the main crack forms in the martensitic phase and grows faster. Meanwhile, the second crack continues to grow at a much slower rate inside the γ-phase. When the second crack crosses the γ-phase boundary into martensitic region, the main crack slows down and eventually stops.

In table 1, compliance components are given. Spaces are left to separate the rows into three groups. The first group gives the results when the main crack advances with an increasing da/dN; the second group is for the slowing main crack, and the last group represents the results when it stops. The results show that as the crack advances, absolute values of compliance components decrease, indicating an increase in stiffness and thus a decrease in fracture resistance. When the crack slows down and finally stops, a_{11} and a_{12} remain stable with other values fluctuating. Some of the a_{66} values in table 1 are negative, indicating that the shear modulus is negative. A negative shear modulus is possible in the presence of martensitic phase transformation [27] and localization.

3.5. Shape memory case

The DIC images show the presence of a straight crack emanating from the notch (initial crack). A second straight crack (effective crack) as shown in figure 20 shows up at around 80 000 loading cycles for which the effective stress intensity factor is calculated as 7.095 MPa$\sqrt{\text{m}}$ at a crack length of

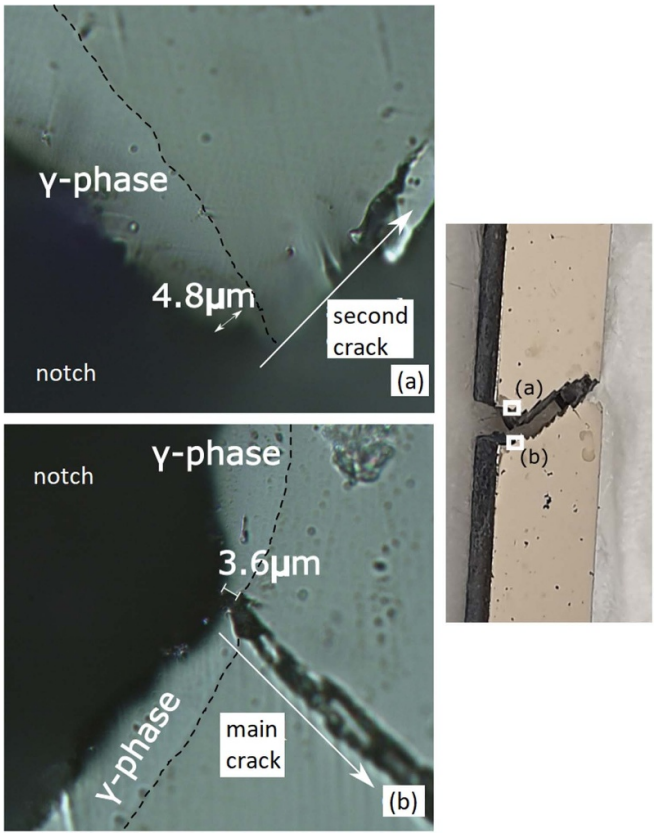


Figure 19. Crack initiation at the notch (SE2). (a) Second crack, (b) main crack. Inset shows the areas which correspond to the microscopic images are taken.

Table 1. Compliance components calculated using equations (1)–(5) (SE2). DIC data are obtained from the AOI in figure 16. a_{ij} are given in 10^{-5} MPa $^{-1}$.

Cycle Number	a (mm)	a_{11}	a_{12}	a_{22}	a_{16}	a_{26}	a_{66}
1	0.0246	7.65	−7.2	12.4	−1.1	3.52	4.93
402	0.0496	5.74	−4.2	8.68	0.685	2.38	5.31
503	0.0710	4.96	−4.3	8.74	−0.15	2.6	4.18
805	0.1256	1.85	−0.52	4.12	0.868	1.07	3.3
856	0.1868	0.259	−0.14	0.959	−0.53	−0.92	1.89
897	0.1875	0.225	−0.13	0.403	−1.3	−4.5	−1.04
948	0.1892	0.244	−0.12	0.564	−2.9	−10.6	−2.62
1009	0.1899	0.25	−0.15	0.198	−2.0	−7.9	−2.01
1171	0.1946	0.221	−0.14	1.96	−6.1	−10.8	18.5
1272	0.1982	0.173	−0.12	−19.5	−4.8	−2.9	−6.4
1413	0.2012	0.243	−0.18	−11.8	−2.3	−2.2	−1.99
1564	0.2012	0.177	−0.17	3.65	−32	−2.2	−120

0.0358 mm. The initial crack at the bottom stops after the initiation of the effective crack at the notch (see figure 21).

The effective crack then grows from 0.0358 mm to 0.1065 mm (first a straight crack until '2' and then kinked to '3' as shown in figure 21) with increasing da/dN and ΔK_{eff} for about 3500 loading cycles (figure 22).

Optical microscopy images taken after failure show a large region of γ-phase around the notch (figure 23) as a result of which both cracks initiate inside the γ-phase, and grow in Mode I at the early stages until they leave the γ-phase region. As shown in figures 23(a) and (b) the crack deviates when its tip crosses the γ/martensite phase boundary, rather than continuing horizontally. Then the crack advances in mixed mode inside the martensitic phase, following the γ-martensite phase boundary.

New cracks that are not connected to the main crack are formed in several instances during testing as sketched in figure 21 ('5', '8', '13'). In figure 24(a), one of the new cracks

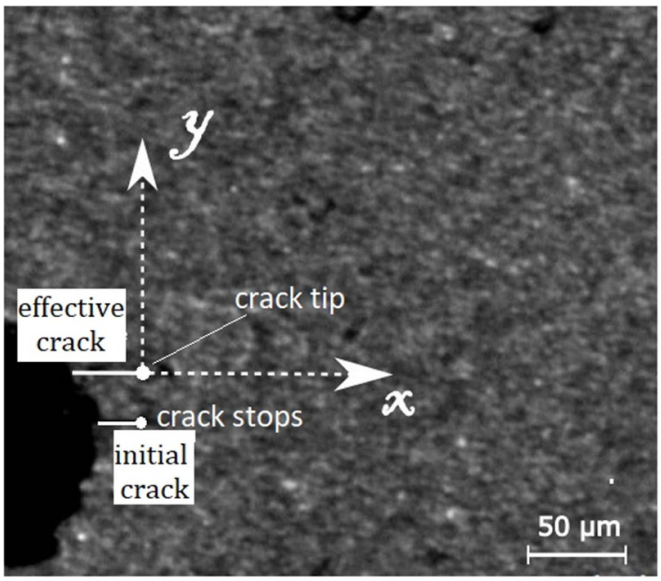


Figure 20. The initial and effective cracks in the shape memory specimen (SM): The effective crack length = 0.0358 mm, $\Delta K_{\text{eff}} = 7.095\,\text{MPa}\sqrt{\text{m}}$.

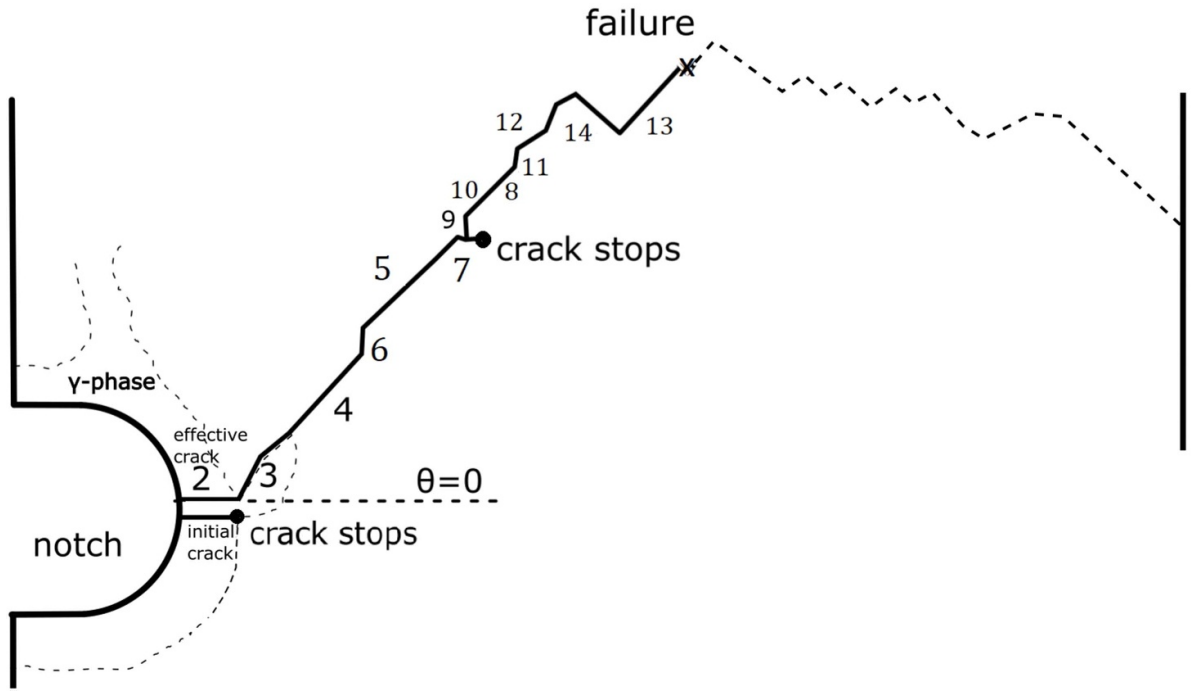


Figure 21. Sketch of the growth path of the effective crack (SM): Numbers indicate the sequences of crack advancement. Dotted line around the notch shows the γ-phase region. The specimen fails after ≈24 000 cycles when the crack length is ≈0.8 mm.

is shown on the DIC image. The new crack is marked '8' to show it is location (figure 24(b)). The length of the effective crack up to '7' in figure 24(a) is 0.5071 mm. Later, as seen in figure 24(b), the crack follows a path towards '9' and the effective crack and the new crack merge at '10'.

In figures 25(a) and (b), optical microscopy shows the presence of the γ-phase where the crack growth slows down and stops. When the growing crack tip '5' hits the non-transforming γ-phase boundary, the crack stops and the effective stress intensity factor decreases. Afterwards the crack advances inside the γ-phase following direction '7' with a slower da/dN and increasing effective stress intensity factor (figure 26). Then a new crack ('8') forms inside the martensitic region, and the effective stress intensity factor decreases. When the crack '8' is closer to '5', the crack through '7' stops, the main crack changes path, follows '9' to '10' and merges with '8' resulting in an increase in the ΔK_{eff} and da/dN (See figure 26).

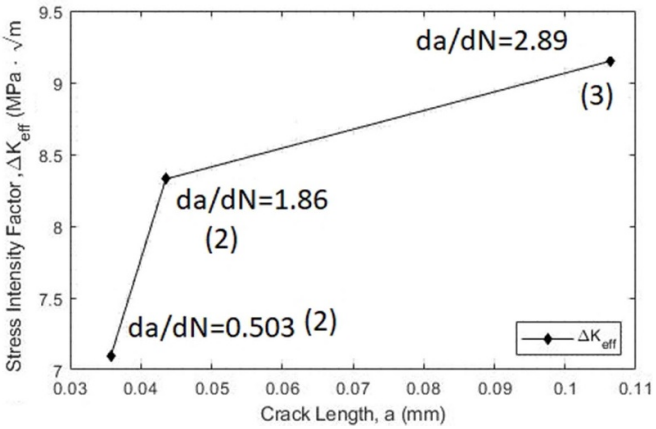


Figure 22. Effective stress intensity factor vs. crack length after crack initiation (SM). Corresponding crack growth rates (da/dN) are given in 10^{-8} m cycle^{-1}. Numbers in parentheses correspond to the crack growth sequences of the effective crack in figure 21.

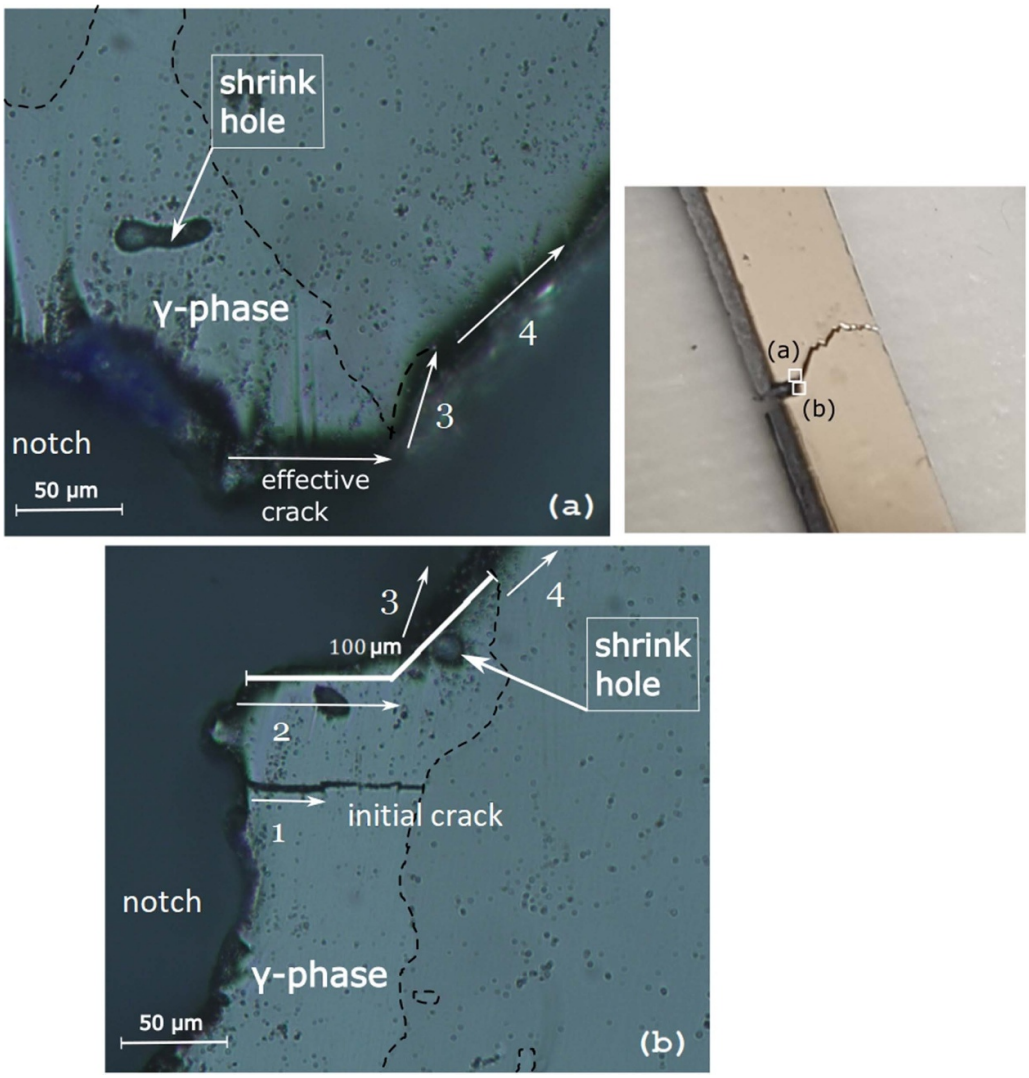


Figure 23. Optical microscopy images around the ruptured notch (a) the top, (b) the bottom (SM). Inset shows the ruptured specimen and the areas to which the microscopic images correspond.

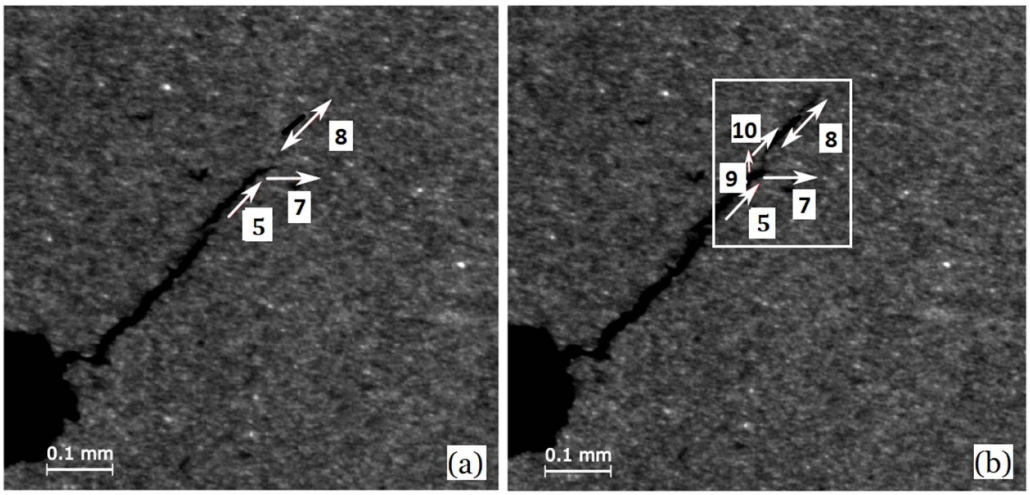


Figure 24. Crack growth in the shape memory specimen (SM). (a) DIC image showing a new crack formation (‘8’). (b) The main crack and the new crack merge.

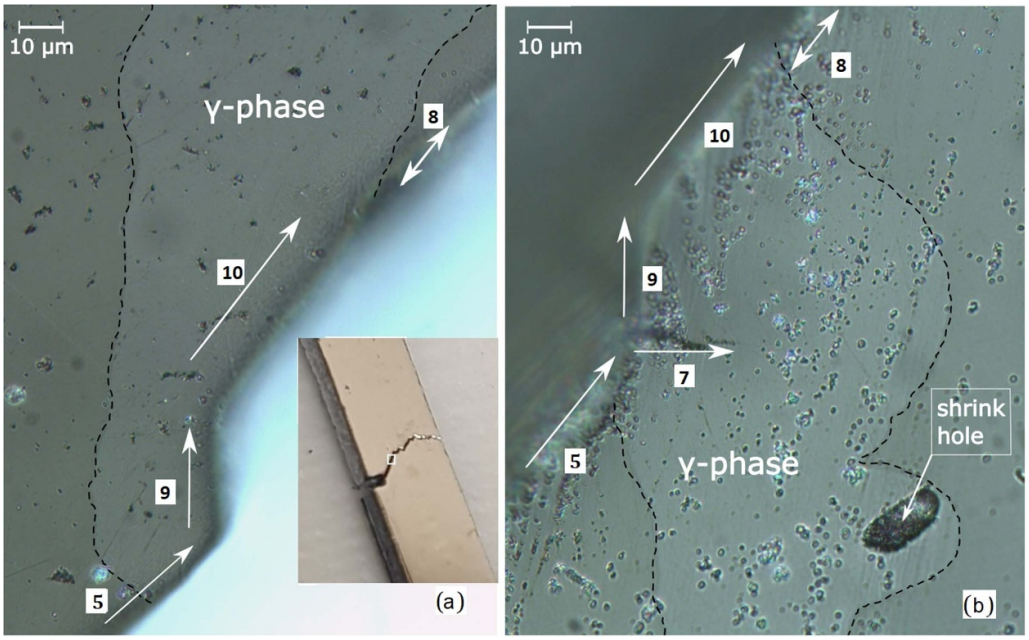


Figure 25. Crack growth in the shape memory specimen (SM). Optical microscopy image taken around the two cracks (‘5’ and ‘8’) that merge at ‘9’ and‘10’: (a) the top, (b) the bottom part of the ruptured specimen. γ-phase borders are shown with black dashed lines. Inset shows the ruptured specimen and the area to which the microscopic images corresponds.

Vertical displacement and ϵ_{yy} strain contours corresponding to figures 24(a) and (b) are presented in figures 27 and 28, respectively. When a new crack forms away from the main crack, vertical displacement and strains around the crack tip decrease, explaining the cause for the low-stress intensity factor in the case of figure 24(a).

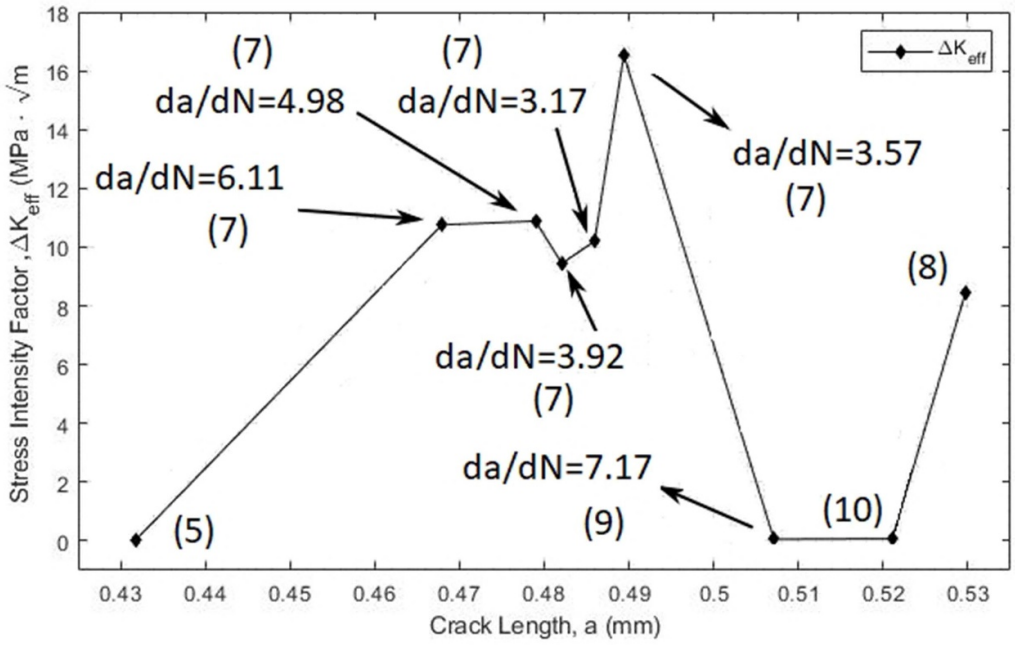


Figure 26. Effective stress intensity factor vs. crack length (SM). Corresponding crack growth rates (da/dN) are given in 10^{-8} m cycle^{-1}. Numbers in parentheses correspond to the crack growth sequences of the effective crack in figure 21.

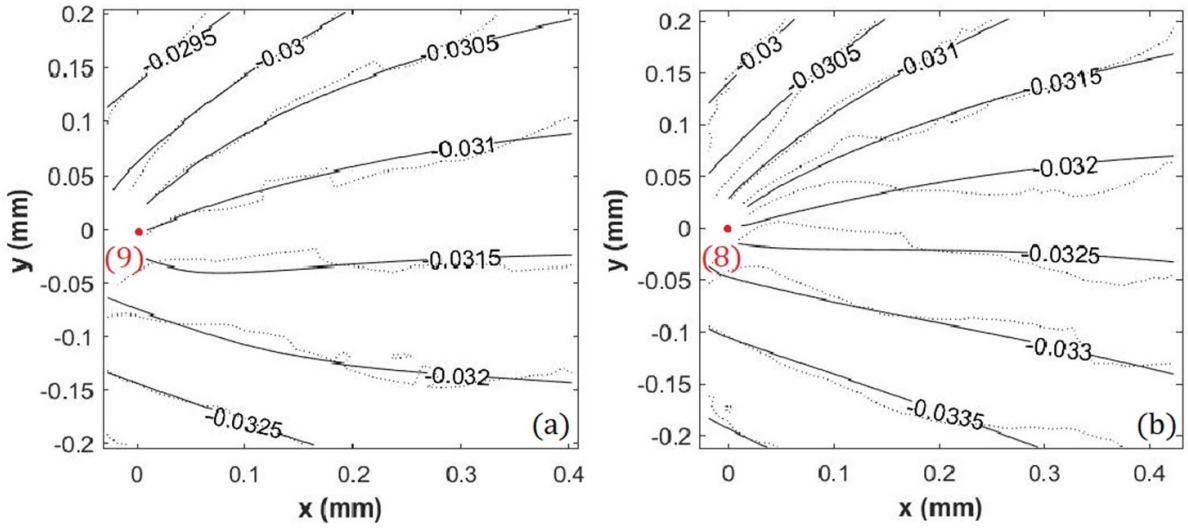


Figure 27. Vertical displacement contours corresponding to (a) figure 24(a), (b) to figure 24(b) (full lines: Δv from equation (2), dotted lines: DIC)(SM).

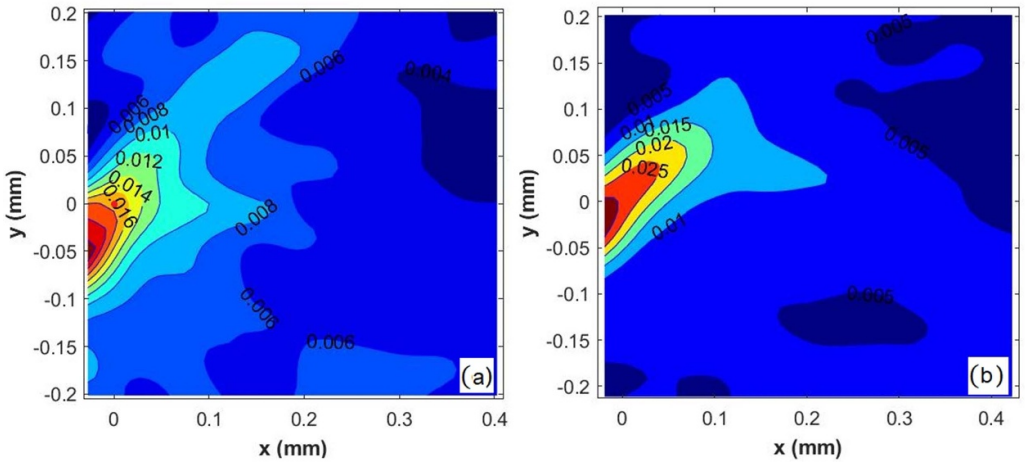


Figure 28. ϵ_{yy} contours corresponding to (a) figure 24(a), and (b) to figure 24(b), respectively (SM).

4. Summary and conclusions

In this work, the purpose was to discuss the fracture behavior of CoNiAl. As a result, the crack growth under cyclic loading in CoNiAl shape memory specimens that have shape-memory behavior at room temperature, and superelastic behavior at 50 °C is studied in detail. Using edge-notched specimens, tests are carried out in superelastic and shape memory regimes, and the effects of the transformation and the secondary phase on crack growth are reported.

The optical microscopy images show the presence of a γ-phase around the notch, the dimensions of which have an effect on crack initiation. Crack initiates after 18 000 loading cycles in the first (SE1), 3000 loading cycles in the second (SE2) superelastic specimen, and after 80 000 loading cycles in the shape memory (SM) specimen, where the thicknesses of the γ-phase regions around the notch are different.

Test specimens that are examined post-failure with optical microscopy show the presence of γ-phase where and when the propagating cracks slow down, deviate, and/or stop. When the crack tip hits the non-transforming ductile γ-phase, first the crack stops, then it continues through the γ-phase with a slower crack growth rate (da/dN). In the meantime, the austenite region outside the γ-phase ahead of the crack tip starts to transform into martensite. During unloading, the reverse transformation is constrained by the γ-phase, a large area of residual martensite remains, in which a new crack forms and starts growing independent from the previous crack. Finally, the ductile γ-phase also cracks and the two cracks merge.

γ-phase formations positioned close to the main propagating crack tip increase the time to failure by blocking crack advancement. The first superelastic specimen and the shape memory specimen have comparable γ-phase volume fractions ahead of the growing crack tip but the shape memory specimen reaches failure after ≈24 000 loading cycles and the first superelastic specimen fails after ≈36 000 cycles which can be explained as a result of the higher number of γ-phase encounters during crack advancement in SE1. γ-phase regions in the first superelastic specimen are smaller in size, but greater in number than the ones in shape memory specimen (See figures 10, 11 and 25). In the second superelastic specimen due to the lack of γ-phase regions close to the main propagating crack tip (figure 17), the main crack grows faster; and reaches failure in a shorter time at only 1664 cycles.

The insets in figures 10, 19 and 25 show zigzags in crack pathways because of microstructural barriers, cracks stop growing or deflect when they reach γ-phase boundaries, the γ-phase regions act as 'barriers' to crack growth.

Ductile secondary phases can stop and deflect a growing crack, or the crack can cut through the secondary phase [28]. The γ-phase is ductile and can deform plastically, absorbing energy and causing the crack to stop at the γ-phase boundary. The γ-phase acts as a microstructural barrier in front of the crack tip. When the γ-phase size is small relative to the crack length, the crack either cuts through or bends around the γ-phase region depending on the stress distribution around the crack tip. If the γ-phase is large, however, it fatigues, and eventually breaks after cyclic loading.

Results of the present study show that the heat-treated CoNiAl has increased resistance to crack growth as a result of crack–γ phase interaction. In the absence of γ-phase the material is more brittle with less fracture resistance. The classical approach of LEFM captures the increase in fracture resistance, but it misses the considerable effect of microstructural behavior (crack interaction with transformed & re-oriented regions, and γ-phase) that is discussed in detail in this paper. One should be cautious with the toughness results reported in the literature.

Data availability statement

The raw/processed data required to reproduce these findings cannot be shared at this time as the data also form part of an ongoing study. They are available from the authors upon request.

Acknowledgments

The authors acknowledge the assistance of S Ravi and J Yaacoub during the experiments done while F Mutlu was a visitor at University of Illinois at Urbana-Champaign, Department of Mechanical Science and Engineering. Prof. Sehitoglu is supported by NSF-DMR - 2104971, Metallic Materials and Nanomaterials Program, which is gratefully acknowledged.

ORCID iD

Fatma Mutlu https://orcid.org/0000-0001-8668-7592

References

[1] Ma Y, Yang S, Liu Y and Liu X 2009 The ductility and shape-memory properties of ni–mn–co–ga high-temperature shape-memory alloys *Acta Mater.* **57** 3232–41
[2] Wu Z *et al* 2019 A eutectic dual-phase design towards superior mechanical properties of heusler-type ferromagnetic shape memory alloys *Acta Mater.* **181** 278–90
[3] Euh K, Lee J-M, Nam D-H and Lee S 2011 In-situ fracture observation and fracture toughness analysis of Ni-Mn-Ga-Fe ferromagnetic shape memory alloys *Metall. Mater. Trans.* A **42** 3961–8
[4] Efstathiou C, Sehitoglu H, Wagoner Johnson A J, Hamilton R F, Maier H J and Chumlyakov Y 2004 Large reduction in critical stress in Co–Ni–Al upon repeated transformation *Scr. Mater.* **51** 979–85
[5] Eftifeeva A S, Yu Panchenko E and Chumlyakov Y I 2015 The effect of thermal cycling and stress-assistant ageing two way shape memory effect in [123] oriented $Co_{40}Ni_{33}Al_{27}$ single crystals *IOP Conf. Ser.: Mater. Sci. Eng.* **71** 012060
[6] Panchenko E, Eftifeeva A, Chumlyakov Y, Gerstein G and Maier H J 2018 Two-way shape memory effect and thermal cycling stability in $Co_{35}Ni_{35}Al_{30}$ single crystals by low-temperature martensite ageing *Scr. Mater.* **150** 18–21
[7] Gerstein G, Firstov G S, Kosorukova T A, Koval Y N and Maier H J 2018 Development of B2 shape memory intermetallics beyond NiAl, CoNiAl and CoNiGa *Shape Mem. Superelasticity* **4** 360–8
[8] Oikawa K, Wulff L, Iijima T, Gejima F, Ohmori T, Fujita A, Fukamichi K, Kainuma R and Ishida K 2001 Promising ferromagnetic Ni–Co–Al shape memory alloy system *Appl. Phys. Lett.* **79** 3290–2
[9] Oikawa K, Omori T, Sutou Y, Kainumal R and Ishidal K 2003 Development of the Co-Ni-Ai ferromagnetic shape memory alloys *J. Phys.* IV **112** 1017–20
[10] Tanaka Y, Ohmori T, Oikawa K, Kainuma R and Ishida K 2004 Ferromagnetic Co–Ni–Al shape memory alloys with $\beta+\gamma$ two-phase structure *Mater. Trans.* **45** 427–30
[11] Hamilton R F, Sehitoglu H, Efstathiou C, Maier H J, Chumlyakov Y and Zhang X Y 2005 Transformation of Co–Ni–Al single crystals in tension *Scr. Mater.* **53** 131–6
[12] Rajini Kanth B, Ramarao N V, Panda A K, Gopalan R, Mitra A and Mukhopadhyay P K 2010 Effect of annealing on the martensitic transformation of a conial ferromagnetic shape memory alloy *J. Alloys Compd.* **491** 22–25
[13] Sutou Y, Kainuma R, Ishida K and Taya M 2003 Martensitic transformation behavior under magnetic field in Co–Ni–Al ferromagnetic shape memory alloys *Smart Structures and Materials 2003: Active Materials: Behavior and Mechanics* vol 5053 (International Society for Optics and Photonics) pp 159–68
[14] Liu J, Zheng H X and Li J G 2006 Effect of solidification rate on microstructure and crystal orientation of ferromagnetic shape memory alloys Co–Ni–Al *Mater. Sci. Eng.* A **438** 1061–4
[15] Eftifeeva A, Panchenko E, Chumlyakov Y and Jürgen Maier H 2017 Two-way shape memory effect in [001] B2-oriented Co–Ni–Al single crystals *Mater. Today Proc.* **4** 4789–96
[16] Tanaka Y, Oikawa K, Sutou Y, Omori T, Kainuma R and Ishida K 2006 Martensitic transition and superelasticity of Co–Ni–Al ferromagnetic shape memory alloys with $\beta+\gamma$ two-phase structure *Mater. Sci. Eng.* A **438** 1054–60
[17] Canadinc D, Dadda J, Jürgen Maier H J, Karaman I, Karaca H E and Chumlyakov Y I 2007 On the role of the cooling rate and crystallographic orientation on the shape memory properties of conial single crystals under compression *Smart Mater. Struct.* **16** 1006
[18] Dar R D and Chen Y 2015 Nanoindentation studies of small-scale martensitic transformations and ductile precipitate effects in dual-phase polycrystalline shape memory alloys *Acta Mater.* **91** 112–27
[19] Dilibal S, Sehitoglu H, Hamilton R F, Maier H J and Chumlyakov Y 2011 On the volume change in Co–Ni–Al during pseudoelasticity *Mater. Sci. Eng.* A **528** 2875–81
[20] Felix Hamilton R F, Sehitoglu H, Efstathiou C, Maier H J and Chumlyakov Y 2006 Pseudoelasticity in Co–Ni–Al single and polycrystals *Acta Mater.* **54** 587–99
[21] Meyer D, Maier H J, Dadda J, Karaman I and Karaca H E 2006 Thermally and stress-induced martensitic transformation in Co–Ni–Al ferromagnetic shape memory alloy single crystals *Mater. Sci. Eng.* A **438** 875–8
[22] Sih G C, Paris P C and Irwin G R 1965 On cracks in rectilinearly anisotropic bodies *Int. J. Fract. Mech.* **1** 189–203
[23] Wu Y, Ojha A, Patriarca L and Sehitoglu H 2015 Fatigue crack growth fundamentals in shape memory alloys *Shape Mem. Superelasticity* **1** 18–40
[24] Sgambitterra E, Maletta C, Furgiuele F and Sehitoglu H 2018 Fatigue crack propagation in [0 1 2] NiTi single crystal alloy *Int. J. Fatigue* **112** 9–20
[25] Anderson T L and Anderson T L 2005 *Fracture Mechanics: Fundamentals and Applications* (CRC Press)
[26] Erdogan F and Sih G C 1963 On the crack extension in plates under plane loading and transverse shear *J. Basic Eng.* **85** 519–25
[27] Jaglinski T, Frascone P, Moore B, Stone D S and Lakes R S 2006 Internal friction due to negative stiffness in the indium–thallium martensitic phase transformation *Phil. Mag.* **86** 4285–303
[28] Kumar S and Curtin W A 2007 Crack interaction with microstructure *Mater. Today* **10** 34–44